In situ visualization of multicomponents coevolution in a battery pouch cell

Guibin Zan[a,1], Guannan Qian[a,1], Sheraz Gul[b], Jizhou Li[a] [ID], Katie Matusik[b], Yong Wang[c], Sylvia Lewis[b], Wenbing Yun[b], Piero Pianetta[a] [ID], David J. Vine[b,2], Linsen Li[c,d,2] [ID], and Yijin Liu[a,2] [ID]

Lithium-ion battery (LIB) is a broadly adopted technology for energy storage. With increasing demands to improve the rate capability, cyclability, energy density, safety, and cost efficiency, it is crucial to establish an in-depth understanding of the detailed structural evolution and cell-degradation mechanisms during battery operation. Here, we present a laboratory-based high-resolution and high-throughput X-ray micro–computed laminography approach, which is capable of in situ visualizing of an industry-relevant lithium-ion (Li-ion) pouch cell with superior detection fidelity, resolution, and reliability. This technique enables imaging of the pouch cell at a spatial resolution of 0.5 μm in a laboratory system and permits the identification of submicron features within cathode and anode electrodes. We also demonstrate direct visualization of the lithium plating in the imaged pouch cell, which is an important phenomenon relevant to battery fast charging and low-temperature cycling. Our development presents an avenue toward a thorough understanding of the correlation among multiscale structures, chemomechanical degradation, and electrochemical behavior of industry-scale battery pouch cells.

lithium-ion battery | in situ three-dimensional imaging | laboratory computed laminography | pouch cell | high resolution

Lithium-ion batteries (LIBs) have become one of the most successful technologies for energy storage. Their broad applications include portable consumer electronics, electric vehicles, and grid energy storage (1–4). With increasing demands to improve the rate capability, cyclability, energy density, and safety of LIBs while decreasing the costs, it is crucial to understand the detailed structural evolution and the cell-degradation mechanisms (1). In addition, LIBs are complex electrochemical systems with hierarchical and multiscale structures in which a collection of physical and chemical processes take place (5). To build better batteries, the electrochemical properties of the battery components should be carefully considered from both thermodynamic (6) and kinetic (7) perspectives. The mechanical stress and thermal behaviors also play important roles during battery operation.

To better understand the battery properties, in situ and/or in operando characterizations are indispensable and, yet, rather challenging. Due to the sophisticated interplay among different cell components, it is highly desirable to simultaneously characterize cathode and anode active materials, carbon-binder-domain, current collector, and other factors. These cell components exhibit very different chemical and physical properties, posing significant challenges for the characterization techniques. Another hurdle lies with the cell architecture. There are many different types of LIB cells used in research setting and in practice. Examples include milliampere hour–level coin cells commonly used in the laboratory, and milliampere-level pouch, prismatic, and cylindrical cells equipped on electric vehicles. A traditional approach for LIB quality inspection is to analyze the voltage and current of the cell. This approach can provide useful insights into many aspects of the battery performance. However, it is a bulk-averaged measurement and neglects all the details regarding the cell structural defects and the heterogeneous chemical processes that occur inside a battery. On the contrary, imaging techniques have been used to investigate the LIB structure and behaviors in two dimensions (2Ds) and three dimensions (3Ds) (8, 9). It is important to point out that the battery performance could be affected by the cell architecture, which could affect the electrochemical impedance, capacity retention, stress, and heat accumulation, among other factors. For example, to facilitate many of the in situ and/or in operando imaging observations, specialized cells with transparent or ultrathin observation windows have been elaborately designed (10). These tailored cells are useful to the mechanistic studies, and the cell design is often determined by the constraints of the characterization technique, which could jeopardize the validity of the electrochemical results (11). Even for well-standardized commercial cells, different performance has been

Significance

Lithium-ion battery is a broadly adopted technology for energy storage. It is crucial to establish an in-depth understanding of the detailed structural evolution and cell degradation mechanisms during battery operation. Here, we develop a high-resolution and high-throughput laboratory-based micro–computed laminography system, which is capable of in situ imaging an industry-relevant large pouch cell at a three-dimensional spatial resolution of 0.5 μm and identifying sub-micron features in multiple cell components. The methodology presents an avenue toward a thorough understanding of the correlation among multiscale structures, chemomechanical degradation, and electrochemical behavior of industry-scale battery pouch cells.

reported in different cell configurations (12). For example, the tab-less 4680 cylindrical cell (i.e., 46 mm in height, 80 mm in diameter) could deliver more capacity in comparison with the conventional 21700 and 18650 cells. This is because the 4680 cells contain smaller amount of inactive materials, thanks to the innovative cell design. Clearly, the ultimate performance of a battery is a combined effect of electrochemistry, interphase chemistry, corrosion, mechanics, thermotic, and cell designs. Therefore, in situ and/or in operando observation of all the cell components in commercial LIB cells is pivotal to battery research and development.

Over the past decade, many advanced imaging techniques have been developed to probe the internal structure and to directly monitor the status of the battery. Here, we survey a few notable examples of the tremendous efforts in this field. Infrared thermography (13, 14), acoustic imaging (15, 16), and X-ray imaging (17, 18) have been used to investigate the industry-scale batteries. Infrared thermal imaging has been used to study the mechanisms of heat generation and material evolution during battery operation and thermal runway. Acoustic imaging is an effective tool to detect the gas generation and electrolyte wetting in the battery. Two-dimensional X-ray radiography has been used for inline inspection and defect analysis in industrial manufacturing (19, 20). Although it provides an opportunity to perform rapid inspections, 2D X-ray radiography lacks the structural information along the beam direction. Another powerful technique widely applied in battery research and development is the X-ray micro–computed tomography (micro-CT), which can reveal the evolutions of the electrode morphology (21), battery structure (22), and state of charge (23) in operating cylindrical cells. However, the laboratory-based X-ray tomographic technique encounters increasing difficulties when applied to the other cell geometries. This is particularly the case for high-aspect-ratio pouch cells. When a micro-CT is used to image a high-aspect-ratio pouch cell, the image contrast is severely deteriorated due to the high absorption of the X-ray along the longitudinal direction (*SI Appendix*, Fig. S1*A*) (24), and the spatial resolution is limited to tens of microns (18, 25) due to the geometrical restrictions (*SI Appendix*, Fig. S1*B*). Consequently, high-throughput, high resolution, laboratory-based, 3D X-ray imaging is yet to be achieved for lithium-ion (Li-ion) pouch cells.

In this work, a laboratory-based high-resolution and high-throughput X-ray micro–computed laminography (micro-CL) is developed for in situ visualization of an industry-relevant Li-ion pouch cell. Multiple cell components including cathode, anode, and plated lithium are imaged and analyzed. Our results clearly demonstrate evidence for a number of degradation processes in a real-world pouch cell. Details regarding the deformation of the battery cathode and anode, the evolving uniformity of cathode particle density, the transition metal dissolution and precipitation, and the lithium plating will be discussed. These unprecedented capabilities, which are not accessible through conventional micro-CT characterizations, could strengthen our understanding of the relationship between the microscopic characterizations and electrochemical measurements for industry-scale Li-ion pouch cells.

Results

High-Resolution Micro-CL Enables Particle-Level Identification.
In a laboratory 3D X-ray imaging system, a short source-to-object distance (SOD) is desired. This is because it not only facilitates a high geometry magnification to achieve high spatial resolution, it also increases X-ray flux on the sample. Small SOD could improve the experimental throughput because the

X-ray flux on a region of interest is inversely proportional to the square of the SOD. In our application, the requirement to rotate a planar sample through 360° sets a lower limit for the SOD and, therefore, limits the throughput of laboratory micro-CT scans. Moreover, it is desirable to maintain a constant effective sample thickness as a function of rotation angle to avoid beam hardening. Beam hardening occurs when the projected thickness of a sample has significant differences for different projection angles and, therefore, the transmitted X-ray spectrum varies, making it difficult to normalize the data and resulting in artifacts in the 3D reconstruction (26, 27). As a result, the conventional micro-CT is not well suited for imaging high-aspect-ratio planar objects (e.g., a Li-ion pouch cell).

To address this challenge, a laboratory-based, high-resolution and high-throughput micro-CL microscope was developed for imaging an industry-relevant Li-ion pouch cell. Unlike micro-CT, in which the rotation axis is perpendicular to the X-ray beam (*SI Appendix*, Fig. S1*B*), in our micro-CL, the X-ray beam has a slant angle of ϕ with respect to the rotation axis (Fig. 1*A*) and a highly efficient flat panel detector (FPD) can be used for 3D imaging of a planar sample at submicron resolution. Through this approach, both challenges discussed above are addressed: 1) the effective sample thickness is approximately constant regardless of the viewing angle, significantly suppressing the radiation hardening and photon-starvation artifacts; and 2) the pouch cell can be placed very close to the laboratory X-ray source (SOD ~0.5 mm), facilitating a high geometric magnification and a high flux efficiency. We demonstrate, using a resolution target, that the instrumental resolution of our system reaches down to ~0.5 μm (*SI Appendix*, Figs. S2 and S3) and a significant improvement in throughput (*SI Appendix*, Fig. S4). More details about the resolution characterizations for our micro-CL imaging system can be found in *Materials and Methods*. Systematic comparison between our micro-CL results and the conventional micro-CT results can be found in the *SI Appendix* and *SI Appendix*, Figs. S5 and S6.

We demonstrate the capability of our micro-CL setup through in situ imaging of an industry-relevant Li-ion pouch cell from the cell level down to the particle level (more experiment details are provided in *Materials and Methods*). It is of practical importance to image multiple cell components simultaneously, which is very challenging due to the significant difference in the physical properties of the LIB components. The representative virtual slices of the $LiNi_{0.83}Co_{0.12}Mn_{0.05}O_2$ (NMC) cathode and the graphite anode are shown in Fig. 1 *B* and *C*, respectively. Although the cathode and the anode exhibit a large difference in their respective mass density and averaged atomic number, both electrodes can be visualized in a single measurement. We plot the intensity histograms of the NMC cathode and graphite anode in Fig. 1*D*. The graphite anode shows a narrow intensity distribution; in contrast, the NMC cathode shows a wider spread. This is because the composite NMC cathode is made of active NMC materials and inactive carbon and binder domains, which are fitted and displayed in Fig. 1*D*. The spatial resolution of our approach is sufficient to resolve important microscopic morphological features (e.g., cracks and voids in individual electrode particles; see insets in Fig. 1 *B* and *C*).

The fidelity of our imaging results is evidenced by the successful segmentation of the two electrode images (right-most panels in Fig. 1 *B* and *C*), which facilitates the quantification of the particle-size distribution in both electrodes (Fig. 1*E*). According to our result, the NMC cathode particles exhibit a broader distribution of the equivalent diameter in comparison
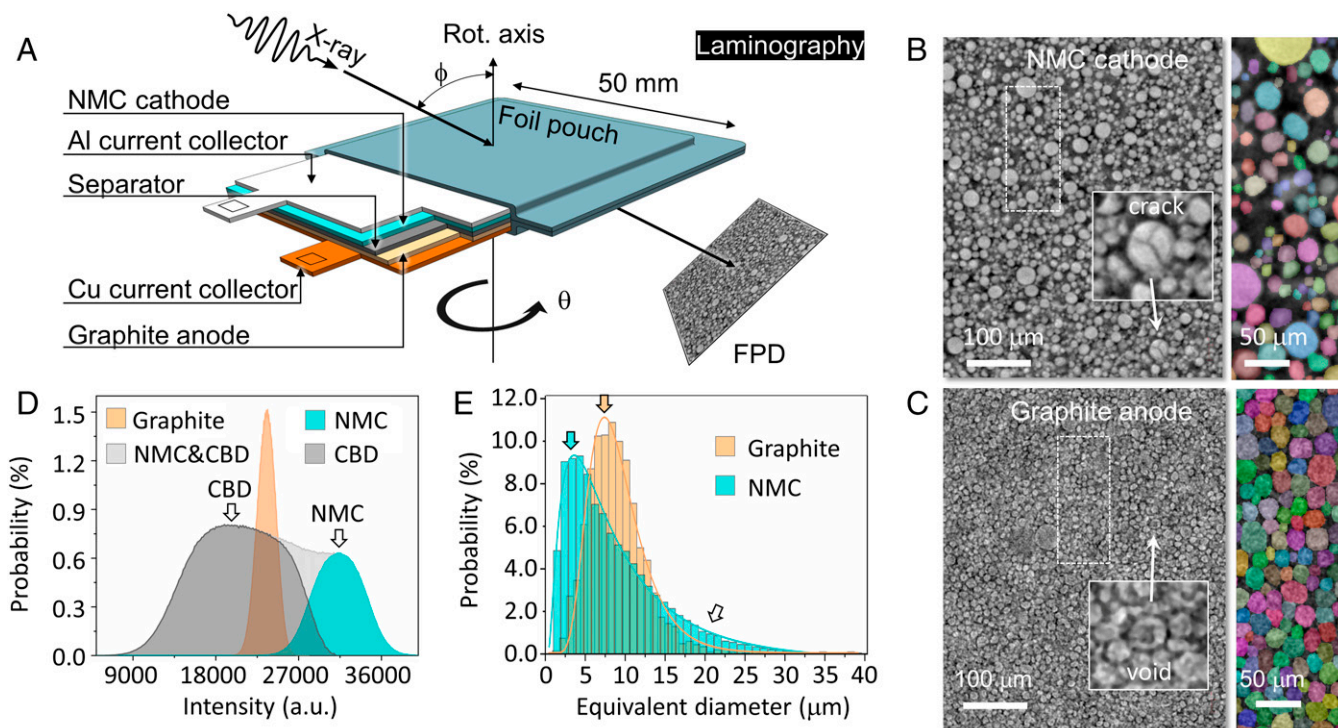
Fig. 1. Micro-CL setup for quantitative in situ imaging of a battery pouch cell. (*A*) A schematic drawing of the developed micro-CL setup for in situ visualizations of a Li-ion pouch cell. (*B* and *C*) Representative slices of the NMC cathode and graphite anode are presented. The insets show the cracks in an NMC particle (*B*) and a void in a graphite particle (*C*). The right-most images in *B* and *C* show the segmented images of two electrodes. (*D*) The intensity histograms of the NMC cathode and graphite anode are shown. (*E*) The equivalent diameters of the particles in these two electrodes are quantitatively analyzed. a.u., arbitrary unit; Rot., rotation.

to that of the graphite anode particles, consistent with the scanning electron microscope (SEM) images (*SI Appendix*, Fig. S7). It is interesting to note that the graphite particles present a fairly symmetry distribution in their size (Fig. 1*E*, yellow arrow). On the contrary, the NMC particle–size distribution is asymmetric, featuring the coexistence of a small number of large NMC particles (Fig. 1*E*, white arrow) and many small NMC particles (Fig. 1*E*, cyan arrow).

Cathode Structural Evolution Upon Cycling. Fig. 2*A* shows a 3D subvolume of the imaged NMC cathode electrode. The coexistence of NMC particles with different sizes is evident and is often adopted for promoting the packing density of the electrode. The same volume was in situ scanned multiple times as the cell was electrochemically charged. Here, we compare two regions of interest at discharged and charged states (Fig. 2 *B, C, E,* and *F*). These two regions of interest feature the electrochemically induced intraparticle heterogeneity (Fig. 2 *B* and *C*) and interparticle heterogeneity (Fig. 2 *E* and *F*), respectively. In Fig. 2*C*, compared with its discharged state (Fig. 2*B*), two bright spots (highlighted in Fig. 2*C* with a yellow arrow and a green arrow) are formed in an NMC particle upon charging. In Fig. 2*F*, the relative intensity inverts between two neighboring NMC particles (highlighted with a purple arrow and a blue arrow). The line profiles in Fig. 2 *D* and *G* also clearly support our assessment of the images. Although the intraparticle and interparticle cathode heterogeneities have been broadly reported (21, 28), our development here highlights the capability of simultaneously in situ imaging many particles, which could allow us to capture the rare events that are sparsely distributed throughout the cathode in a large pouch cell.

In addition to the particle-level analysis, we further performed a deformation analysis on a subvolume of the imaged

NMC cathode (Fig. 2*H*) by applying the standard 3D Lucas–Kanade method (29, 30). To evaluate the particle-size–dependent deformation of the cathode electrode, we separated the cathode particles into two groups: large (Fig. 2*I*) and small (Fig. 2*J*) particles. The deformation trajectory is quantified, and its angles and amplitudes are subsequently extracted from the 3D vectors for each voxel. We compared the in-plane and out-of-plane components by decomposing the deformation vectors based on their moving directions, as demonstrated in Fig. 2*K*. While both large and small particles show a similar relative shift at the in-plane direction (horizontal direction in Fig. 1*A*), the large particles undergo a large relative shift at the out-of-plane direction. The particle-size–dependent deformation behavior is an interesting observation and shall be considered when manufacturing the composite electrode. The mismatched deformation could lead to decohesion of the particle from the carbon and binder domains, which would increase the impedance and degrade the rate performance. The selection of active cathode particles with uniform size distribution could be beneficial in this perspective.

Graphite Anode Particle Deformation Upon Cycling. It is the general consensus that X-ray imaging of graphite anode is more challenging because of its low atomic number and thus low X-ray attenuation. This is particularly the case when imaging the LIB in a full cell configuration, due to the coexistence of multiple cell components. Our micro-CL design enables a small SOD and increases the X-ray flux, which facilitate the in situ imaging of graphite anode.

In Fig. 3, we display several microscopic defects that are formed upon charging. These defects include voids, cracks, and debonding (Fig. 3 *A–C*) of the graphite particles in comparison to their respective discharged status (*SI Appendix*, Fig. S8 *A–C*).
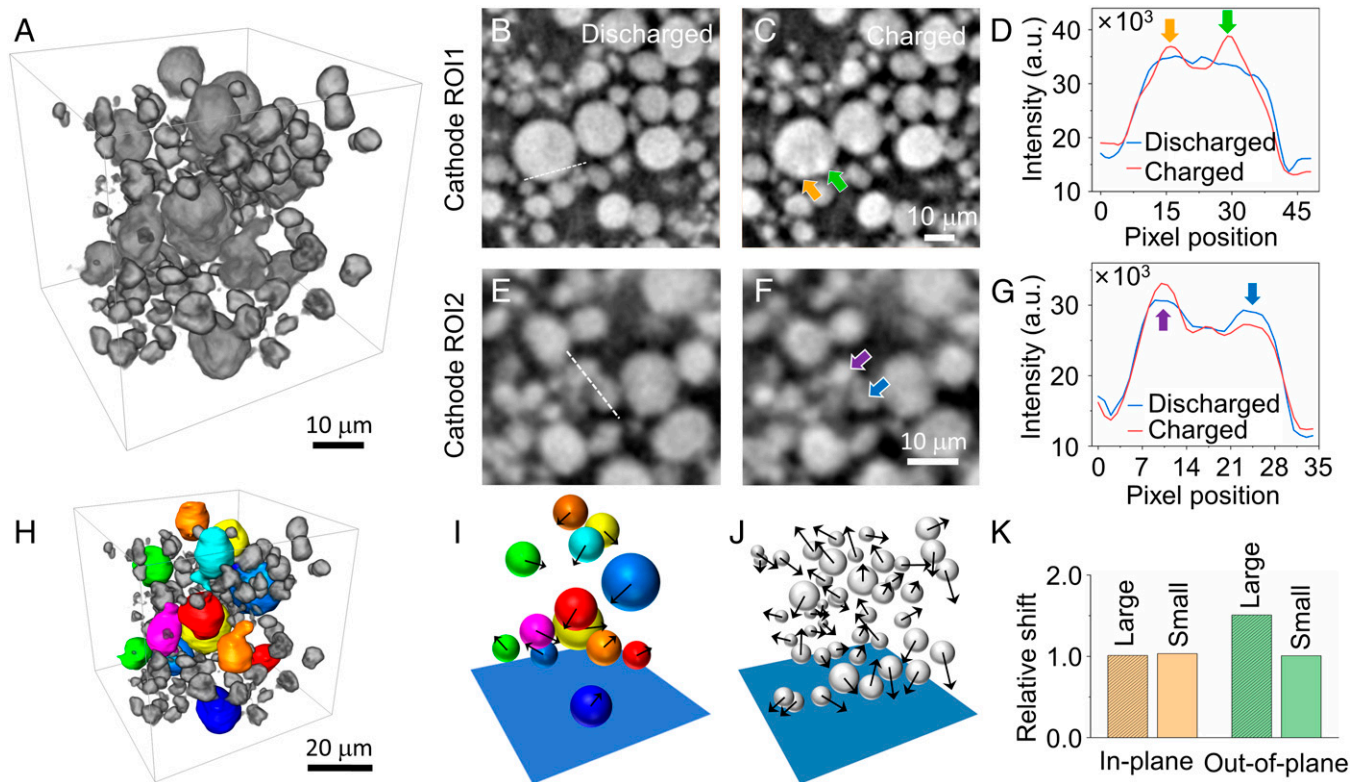
Fig. 2. In situ micro-CL imaging of the NMC cathode. (*A*) 3D rendering of a subvolume of the imaged composite NMC cathode. The intraparticle (*B* and *C*) and interparticle (*E* and *F*) heterogeneities are developed upon charging. The line profiles over the particles in *B* and *C* are shown in *D*, and those over the particles in *E* and *F* are shown in *G*. (*H*) The cathode particles are separated into two groups: large (bright colors) and small (gray). (*I* and *J*) The electrode deformation over the large-size group (*I*) and the small-size group (*J*). (*K*) The relative shifts of these two groups of particles in the in-plane and the out-of-plane directions. a.u., arbitrary unit.

We further segmented three randomly selected graphite particles and quantified the deformation at the particle level. Fig. 3 *D–F* shows that the deformation of these particles is very nonuniform, featuring considerable heterogeneities in both the deformation amplitudes and orientations (arrows in Fig. 3 *D–F*). The averaged amplitude of the deformation vectors over these particles is similar. The probability distributions of the deformation amplitude exhibit a peak at ~1.0 μm (Fig. 3*G*), which is close to 10% of the particle size. As reported, the charging-induced change in graphite's interlayer distance is ~10%, in qualitative agreement with our results (31–33). Furthermore, it is interesting to note that the deformation amplitude in the in-plane direction is larger than in the out-of-plane direction (Fig. 3*H*). A possible reason for this phenomenon is that two layers of carbon fiber–reinforced polymers (CFRPs) were used to fix the pouch cell during the electrochemical cycling. The two layers of CFRPs offer a mechanical force to suppress the expansion in the out-of-plane direction. The stack pressure plays an important role in liquid and solid batteries. Traditionally, it is expected that the pressure mainly modulates interface (34). Our findings highlight that the pressure may also influence the deformation behavior of active anode particles, which is a long-overlooked phenomenon that could affect the electrochemistry of the LIB.

Direct Observation of Multiple Degradation Processes in an Li-ion Pouch Cell. Degradation in LIBs is the consequence of a complicated interplay among a number of chemical and physical processes. Direct observation of multiple degradation processes in their inherent structural and chemical states during battery operation is of vital importance. It could provide an

in-depth and intuitive understanding of their effects on the electrochemical performance and LIB lifetime (35). In many reports in the literature, authors aimed to perform failure analysis by connecting the macroscopic-scale LIB behavior with the microscale characteristics. Direct observation at high resolution, however, usually limits the sample size, due to experimental constraints, which makes it difficult for industry-scale large Li-ion pouches.

By virtue of 3D nondestructive detection using the micro-CL microscope, we demonstrate in situ visualization of an industry-relevant large Li-ion pouch cell. We have systematically presented experimental evidence for the chemomechanical degradations in the cathode of our pouch (e.g., particle cracking; Fig. 4*A*), intraparticle and interparticle heterogeneity (Fig. 4 *B* and *C*), and cathode electrode deformation. The graphite anode particles are imaged simultaneously and their deformation (Fig. 4*D*), void formation, cracking, and debonding are visualized and quantified in situ. The structural deformation and particle pulverization are critical issues in high-capacity electrodes. Visualizing this process could provide valuable insights to inform the particle synthesis and electrode manufacturing.

In addition, after a thorough data review, we captured the formation of several metal particles in the graphite anode upon battery cycling (Fig. 4*E* and *SI Appendix*, Fig. S9*B*). This is attributed to the transition metal dissolution (from the cathode), migration (through the electrolyte), and precipitation (on to the anode). To verify their composition, we conducted micro–X-ray fluorescence (micro-XRF) mapping (*SI Appendix*, Figs. S10 and S11), SEM, and energy dispersive X-ray spectroscopy (EDS) characterization (*SI Appendix*, Figs. S12 and S13). More details about micro-XRF, SEM, and EDS can be found
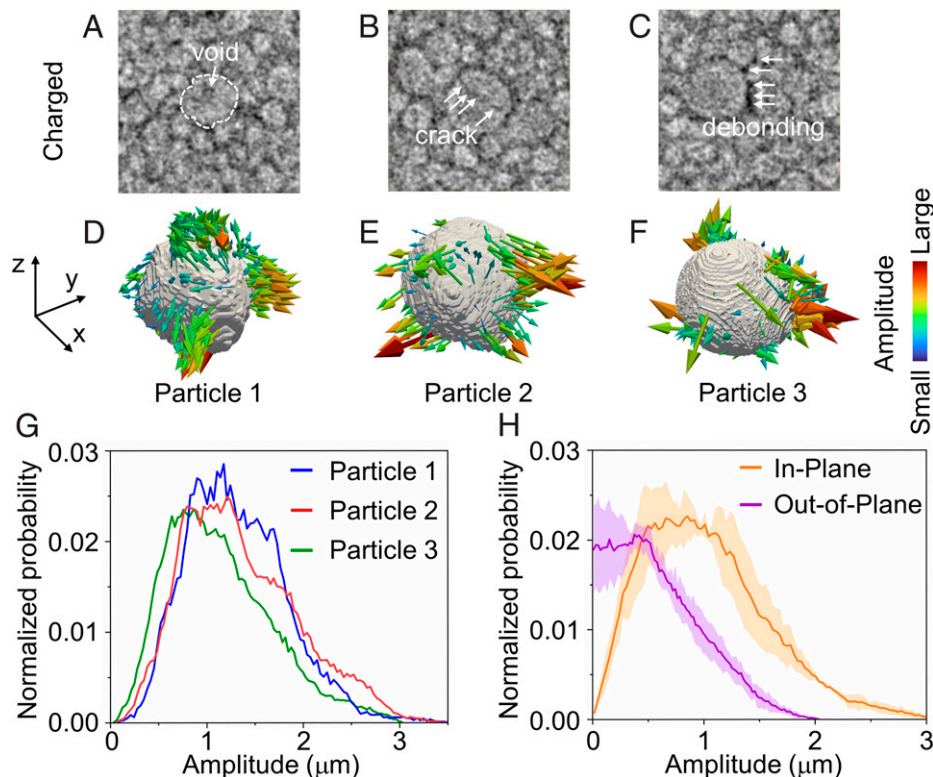
Fig. 3. Deformation analysis at the particle level for the graphite anode. (*A*–*C*) The microscopic defects developed upon charging: voids (*A*), (*B*) cracks, and (*C*) debonding of graphite particles. (*D*–*F*) The charging-induced 3D deformation of three segmented graphite particles. (*G*) The normalized probability distribution of the total deformation amplitude of the three particles. (*H*) The normalized probability distribution of the deformation amplitude in the in-plane and the out-of-plane directions.

in the *SI Appendix*. The fluorescence signals from nickel, cobalt, and manganese are all observed in micro-XRF and/or EDS, respectively. The dissolution–migration–precipitation process is directly related to the capacity fade of the battery and direct in situ observation of this process could be useful to the design of the mitigating approach (36).

Moreover, we report the direct visualization of lithium plating on our anode surface (Fig. 4*F* and *SI Appendix*, Fig. S9*C*), and the lithium plating leads to the consumption of the lithium inventory and thus causes accelerated capacity fade and formation of new solid electrolyte interphase (37). To further confirm the lithium plating, we disassembled the pouch cell in an argon-filled glovebox. *SI Appendix*, Fig. S14 presents a picture of the anode after teardown of the cell, in which the lithium plating regions clearly show a silver and gold coloration. Our micro-CL method could facilitate the investigation of the Li plating behaviors during fast charging or overcharge abuse. To this end, through a single measurement using this micro-CL approach, we have demonstrated direct experimental evidence relevant to multiple degradation processes (schematically illustrated in Fig. 4*G*) that occur in an industry-relevant large Li-ion pouch.

Discussion

In this work, we present noninvasive in situ assessment of an industry-relevant Li-ion pouch cell. Specifically, we developed a high-resolution and high-throughput, laboratory-based micro-CL system, which is capable of imaging the pouch cell at a 3D voxel resolution of 0.5 μm and identifying submicron features in different cell components. This method provides an opportunity to visualize various chemomechanical degradation processes in the

pouch cell, including the deformation of the battery cathode and anode, the evolving uniformity of cathode particle density, the transition metal dissolution and precipitation, and the lithium plating. The sophisticated multicomponent interplay within a functioning industry-relevant battery cell is of fundamental importance to LIB research and development. The methodology we developed presents an avenue toward a thorough understanding of the correlation among multiscale structures, chemomechanical degradation, and electrochemical behavior of industry-scale Li-ion pouch cells.

In the present study, we demonstrated the development by imaging a single-layer pouch cell. We acknowledge that, for battery industry, it is technically important to investigate multi-layer pouch cells. Although our method can potentially be applicable to thick samples, it worth noting that there are two limiting factors that need to be considered and addressed.

First, the micro-CL method has a limited depth of focus and the sample regions outside of the depth of focus could suffer from reduced effective resolution. This limitation could potentially be addressed by a focus-stacking approach, which has been demonstrated in optical microscopy and full-field X-ray microscopy. The adoption of the focus-stacking approach for laminography has not be demonstrated and is a topic of great interest for future research efforts.

Second, the absorption contrast (μ) negatively correlates with the X-ray energy (μ ∝ $1/E^3$, where E is X-ray energy) and positively correlates with the material density and atomic number (μ ∝ ρZ^4, where ρ is the material density and Z is the atomic number) (38). The X-ray energy, material density, and atomic number dependences mean that materials with low atomic number exhibit low X-ray attenuation. In order to investigate a thick sample, high-energy
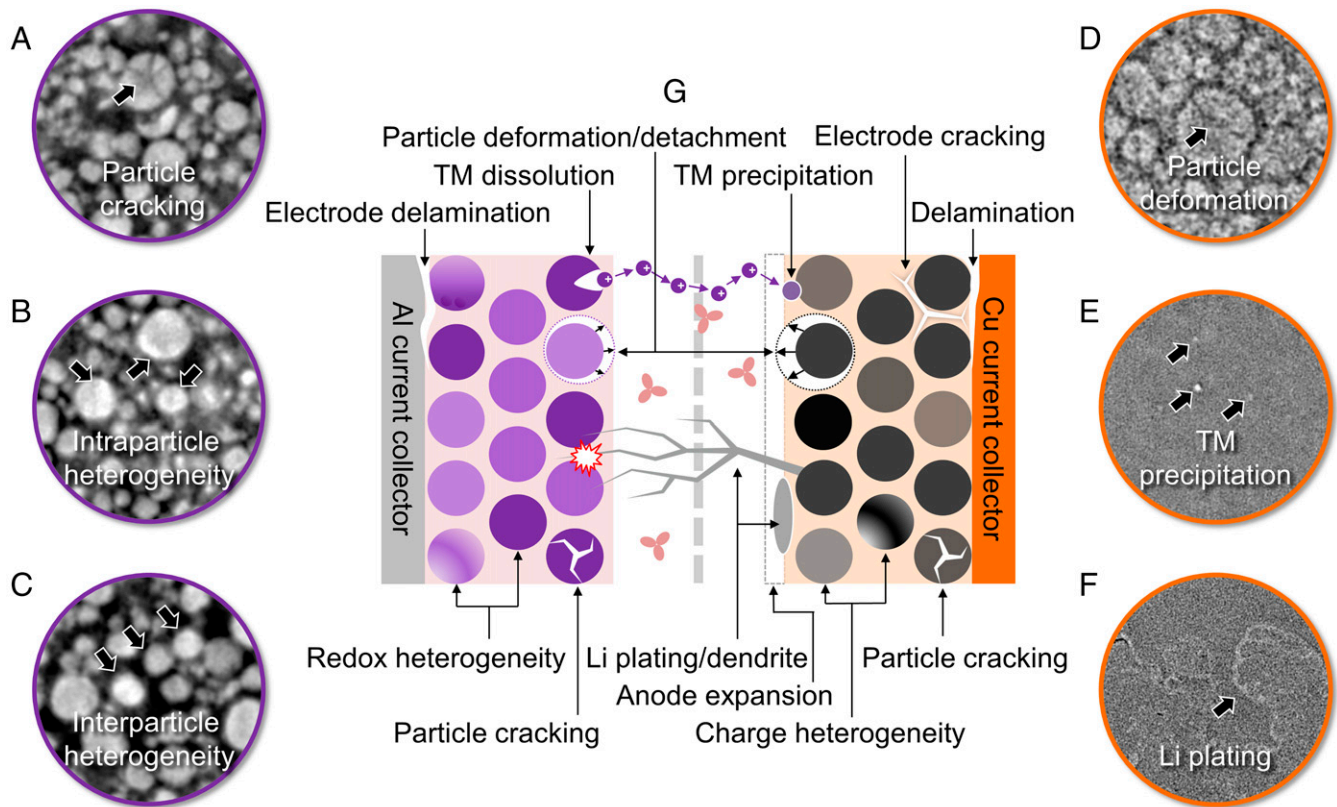
Fig. 4. In situ visualization of multiple degradation processes in an industry-relevant pouch cell. (*A–C*) The chemomechanical degradation occurred in an NMC cathode, including particle cracking (*A*), intraparticle heterogeneity (*B*), and interparticle heterogeneity (*C*). (*D–F*) The degradation occurred in the graphite anode, including particle deformation (*D*), TM precipitation (*E*), and Li plating (*F*). (*G*) Schematics of multiple degradation mechanisms observed in an industry-relevant, large Li-ion pouch cell. TM, transition metal.

X-rays are needed to ensure the penetration. However, the use of high-energy X-rays also leads to poor imaging contrast on the low-Z materials. One possible solution is to integrate the micro-CL system with Talbot interferometry to offer different contrast modalities, which could enhance the sensitivity of this method in imaging low-Z cell components (39). This is a rather sophisticated approach and is clearly beyond the scope of the present article.

The implementation of micro-CL reduces the artifacts of the radiation hardening and photon starvation, which is severe in micro-CT when a high-AR planar object is imaged. However, micro-CL still suffers from a missing cone of data in the reciprocal space, which leads to an anisotropic resolution. Advanced iterative algorithms have been developed to address this, and novel machine-learning developments could potentially be leveraged (40).

Further improvement of the experimental throughput is highly desirable for LIB research, in particular for studies relevant to LIB fast charging. Currently, our 3D reconstruction process utilizes a modified, filtered, back-projection algorithm, which needs a high angular-sampling rate. State-of-art iterative algorithms can be implemented to facilitate the reconstruction with fewer projections, which would, in turn, improve the experimental throughput (24, 41). These iterative algorithms, however, are often computationally expensive, and novel memory-management methods could be a viable approach in this regard. From the hardware perspective, it could be beneficial to integrate the state-of-the-art photon-counting detectors for reducing the image noise.

Beyond the measurement of the Li-ion pouch, the implantation of laboratory-scale micro-CL is applicable rather broadly

for medical, scientific, or engineering problems, where the samples are planar. In particular, this technique is useful to image the integrated circuits in electronics devices for failure analysis, design validation, and quality control.

Materials and Methods

Resolution Characterizations of the Laboratory-Based Micro-CL. Prior to imaging the real-world specimens, we carefully characterized the new micro-CL setup in several key aspects that are crucial to image the pouch cells. The spatial resolution determines the smallest features which can be resolved in the sample. We performed the spatial resolution characterizations with a resolution target, which features an array of precisely controlled, microstructure, tungsten-metal inserts that are embedded in a diamond substrate. Because of the large size of the resolution target (42), two measurements were carried out to image the different scale of line pairs. In the first micro-CL measurement, the SOD was 3.9 mm. The object-to-detector distance (SDD) was 640.5 mm. Paired with 49.5 μm of the pixel size of the FPD, the magnification of 164.2 in the first configuration provided the voxel size of 0.3 μm. In the second micro-CL measurement, a shorter SOD was set as 2.5 mm. The SDD was set as 639.5 mm. The larger magnification of 255.8 in the second configuration provided the voxel size of 0.2 μm. The X-ray voltage of the X-ray source was set as 40kV and the power was 3.0 W. The exposure time was 2.4 s/projection, and 721 X-ray transmission images were acquired for rotation over 360° for both measurements. The collected projection data sets were fed into a modified Feldcamp–Davis–Kress algorithm to reconstruct the 3D volume (24). *SI Appendix*, Fig. S2 shows the reconstructed virtual slice of the first measurement, in which a 1.0-μm line and 0.75-μm line are clearly resolved with a high contrast. *SI Appendix*, Fig. S3 demonstrates the reconstructed virtual slice of the second measurement, in which a 0.5-μm line was probed with moderate contrast. Based on the resolution characterizations, the reconstructed virtual slices and line profiles clearly demonstrate

the spatial resolution of the new laboratory-based micro-CL system can reach 0.5 µm. It be should pointed out that some different kinds of architectures have been developed to carry out the CL technique with a laboratory-scale microfocus source. However, the spatial resolution of the prior-of-art laboratory CL is limited to a few to tens of micrometers (24, 41, 43, 44). We acknowledge that the advent of a synchrotron source pushes the spatial resolution of CL to submicrometers (26, 27), even tens of nanometers are achieved with ptychography scan (40). Nevertheless, the limited access of the synchrotron makes CL technique not broadly available for industry.

Micro-CL Measurement Optimization for Pouch Cell. In our setup, the slant angle, ϕ, can be adjusted by rotating the FPD to fit the geometry configuration. Choosing the slant angle requires a balance between minimizing the missing Fourier space cone and providing sufficient transmission through the sample. To maximize the image quality of the electrode particles, two slant angles have been employed for comparison. The first measurement was carried out with a slant angle of 15°. The exposure time was 6 s/projection; the exposure interval of the angle was 0.1° for the rotation over 360°. The voxel size of the reconstructed 3D image was 0.7 µm. The second measurement was performed by setting the slant angle to 30°. The exposure time was 2 s/projection; the exposure interval of the angle was 0.075° for the rotation over 360°. The voxel size of the reconstructed 3D image was 0.5 µm. Compared with the situation of a slant angle of 15°, X-ray photons go through a short travel range in the sample for the slant angle of 30°, resulting in a higher flux on detector and short exposure time. To pursue a high signal-to-noise ratio, the operating voltage of the source in two measurements was set as 50 kV, which maximized the contrast by optimizing the X-ray transmission (45). *SI Appendix*, Figs. S15 and S16 present the virtual slices of the NMC cathode and graphite anode, respectively. Even though, in both measurements, NMC and graphite can be detected, the contrasts are a bit different. The power spectral density was carried to evaluate these two different measurements, as shown in *SI Appendix*, Figs. S15*E* and S16*E*. The results suggest that the measurements with a slant angle of 30° outperforms in imaging both anode and cathode particles.

To balance the measurement efficiency and performance, the trade-off between the spatial resolution, acquisition time, and the pouch cell volume should be considered. In this study, we chose a slant angle of 30° for all the pouch cell measurements with voxel size of 0.5 µm. The exposure time was 2 s/projection; the exposure interval of the angle was 0.075° for the rotation over 360°. The voltage was set as 50 kV.

High Detector Efficiency in Micro-CL. Typically, the state-of-art laboratory X-ray micro-CT system can achieve a resolution of ~1.0 µm by employing a microfocus X-ray source combined with a scintillator-coupled objective lens and a charge-coupled-device detector with submicron resolution (46, 47). A scintillator (e.g., cesium iodide [CsI] thallium) are coupled on the objective lens to transform the X-rays to visible light, which is collected by an objective lens and imaged onto the charge-coupled device. The thickness of the scintillator governs the fractional absorption of X-rays; consequently, it determines the efficiency of the entire X-ray detector. Despite that, in principle, the thicker scintillator facilitates higher efficiency, in practice, the objective lens has a fixed depth of field in which the entire scintillator must reside to avoid blurring, limiting the thickness of the scintillator (i.e., CsI; e.g., ~30 µm for a 20X objective lens, ~10 µm for 40X objective lens). It should be noted that the thin scintillators are inefficient at

converting high-energy X-rays to visible light, due to insufficient absorption. The implementation of the proposed micro-CL employs a highly efficient FPD, which adopts a thicker CsI with a thickness of 450 µm. The fractional absorption of different thicknesses of CsI scintillator are plotted as a function of X-ray energy in *SI Appendix*, Fig. S4A. While the fractional absorption of the CsI scintillator in an FPD is 0.84, the fractional absorption of the CsI scintillator in a 20X objective lens–coupled indirect detector is 0.12 when 30 keV X-rays are used. The 7.0X higher efficiency gain of an FPD leads to superior imaging throughput in a micro-CL system. *SI Appendix*, Fig. S4B shows the efficiency gains of an FPD over indirect X-ray detectors coupled with the 20X and 40X objective lenses as a function of X-ray energy. The X-ray FPD holds a higher efficiency over the X-ray energy range of 5 to 120 keV, and even higher at high X-ray energies. Therefore, the throughput of the proposed micro-CL improves a lot by using highly efficient FPD for pursuing a submicron resolution.

Cell Preparation. A pouch-type cell was assembled with a single-layer-electrode stack structure. The cell was composed of a 70-µm NMC cathode on an Al current collector, a 50-µm artificial graphite anode on a Cu current collector, and a polyethylene separator. The cell was dried at 85 °C under vacuum for 12 h before filling an electrolyte composed of 1.2 M LiPF$_6$, ethylene carbonate:dimethyl carbonate:diethyl carbonate = 1:1:1 (by weight), and 1.5 wt% vinylene carbonate additive in an argon-filled glovebox (Mikrona; O$_2$/H$_2$O < 0.1 ppm). The electrochemical measurements were performed using a battery cycler (Shenzhen Neware, BTS9000-5V; or Biologic SP300). The more-specific parameters of the cell can be found in *SI Appendix*, Table S1. The cell was first cycled with a current of 5 mA at 2.7 to 4.25 V twice. After that, the cell was abused with a current of 25 mA at 2.7 to 4.9 V three times and then stopped at the specific voltage before further characterizations. *SI Appendix*, Fig. S17A shows the capacity calibration of the pouch cell with a current of 5 mA at 2.7 to 4.25 V. *SI Appendix*, Fig. S17*B* shows the overcharge electrochemical profiles of the pouch cell with a current of 25 mA. After being charged to 4.9 V, the cell is continuously charged with a constant voltage until reaching the limit current of 10 mA. The pouch cell is placed between two CFRPs to compress the cell.

Data Availability. All study data are included in the article and/or supporting information.

Author affiliations: [a]Stanford Synchrotron Radiation Lightsource, SLAC National Accelerator Laboratory, Menlo Park, CA 94025; [b]Sigray Inc., Concord, CA 94520; [c]Department of Chemical Engineering, Shanghai Electrochemical Energy Device Research Center, School of Chemistry and Chemical Engineering, Shanghai Jiao Tong University, Shanghai 200240, China; and [d]Fujian Science & Technology Innovation Laboratory for Energy Devices of China (21C LAB), Ningde, 352100, China

1. N. Nitta, F. Wu, J. T. Lee, G. Yushin, Li-ion battery materials: Present and future. *Mater. Today* **18**, 252–264 (2015).
2. M. Li, J. Lu, Z. Chen, K. Amine, 30 Years of lithium-ion batteries. *Adv. Mater.* **30**, e1800561 (2018).
3. Z. P. Cano *et al.*, Batteries and fuel cells for emerging electric vehicle markets. *Nat. Energy* **3**, 279–289 (2018).
4. Y. Ding, Z. P. Cano, A. Yu, J. Lu, Z. Chen, Automotive Li-ion batteries: Current status and future perspectives. *Electrochem. Energy Rev.* **2**, 1–28 (2019).
5. J. B. Goodenough, K.-S. Park, The Li-ion rechargeable battery: A perspective. *J. Am. Chem. Soc.* **135**, 1167–1176 (2013).
6. Y. Zhao *et al.*, A review on modeling of electro-chemo-mechanics in lithium-ion batteries. *J. Power Sources* **413**, 259–283 (2019).
7. L. Spitthoff, P. R. Shearing, O. S. Burheim, Temperature, ageing and thermal management of lithium-ion batteries. *Energies* **14**, 1248 (2021).
8. Z. Deng *et al.*, Recent progress on advanced imaging techniques for lithium-ion batteries. *Adv. Energy Mater.* **11**, 2000806 (2021).
9. A. J. Ilott, M. Mohammadi, H. J. Chang, C. P. Grey, A. Jerschow, Real-time 3D imaging of microstructure growth in battery cells using indirect MRI. *Proc. Natl. Acad. Sci. U.S.A.* **113**, 10779–10784 (2016).
10. S.-M. Bak, Z. Shadike, R. Lin, X. Yu, X.-Q. Yang, In situ/operando synchrotron-based X-ray techniques for lithium-ion battery research. *NPG Asia Mater.* **10**, 563–580 (2018).
11. C. Tan *et al.*, Evolution of electrochemical cell designs for in-situ and operando 3D characterization. *Materials (Basel)* **11**, 2157 (2018).
12. J. B. Quinn, T. Waldmann, K. Richter, M. Kasper, M. Wohlfahrt-Mehrens, Energy density of cylindrical Li-ion cells: A comparison of commercial 18650 to the 21700 cells. *J. Electrochem. Soc.* **165**, A3284 (2018).
13. S. Goutam, J.-M. Timmermans, N. Omar, P. V. d. Bossche, J. Van Mierlo, Comparative study of surface temperature behavior of commercial Li-ion pouch cells of different chemistries and capacities by infrared thermography. *Energies* **8**, 8175–8192 (2015).
14. S. Wang *et al.*, Infrared imaging investigation of temperature fluctuation and spatial distribution for a large laminated lithium–ion power battery. *Appl. Therm. Eng.* **152**, 204–214 (2019).
15. Z. Deng *et al.*, Ultrasonic scanning to observe wetting and "unwetting" in Li-ion pouch cells. *Joule* **4**, 2017–2029 (2020).
16. W. Chang, D. Steingart, Operando 2D acoustic characterization of lithium-ion battery spatial dynamics. *ACS Energy Lett.* **6**, 2960–2968 (2021).

17. D. P. Finegan et al., In-operando high-speed tomography of lithium-ion batteries during thermal runaway. *Nat. Commun.* **6**, 6924 (2015).
18. C. Chen, Y. Wei, Z. Zhao, Y. Zou, D. Luo, Investigation of the swelling failure of lithium-ion battery packs at low temperatures using 2D/3D X-ray computed tomography. *Electrochim. Acta* **305**, 65–71 (2019).
19. A. Schilling et al., X-ray based visualization of the electrolyte filling process of lithium ion batteries. *J. Electrochem. Soc.* **166**, A5163 (2018).
20. G. Qian et al., The role of structural defects in commercial lithium-ion batteries. *Cell Rep.* **2**, 100554 (2021).
21. G. Zan et al., Understanding multi-scale battery degradation with a macro-to-nano zoom through its hierarchy. *J. Mater. Chem. A Mater. Energy Sustain.* **9**, 19886–19893 (2021).
22. M. T. M. Pham et al., Prevention of lithium-ion battery thermal runaway using polymer-substrate current collectors. *Cell Rep.* **2**, 100360 (2021).
23. M. J. Mühlbauer et al., Inhomogeneous distribution of lithium and electrolyte in aged Li-ion cylindrical cells. *J. Power Sources* **475**, 228690 (2020).
24. S. L. Fisher et al., Laminography in the lab: Imaging planar objects using a conventional x-ray CT scanner. *Meas. Sci. Technol.* **30**, 035401 (2019).
25. T. Fras, P. Pawlowski, W. Li, T. Wierzbicki, Performance of Li-ion pouch battery under a high-velocity impact: Experiment and numerical simulation. *Int. J. Impact Eng.* **155**, 103915 (2021).
26. L. Helfen et al., High-resolution three-dimensional imaging of flat objects by synchrotron-radiation computed laminography. *Appl. Phys. Lett.* **86**, 071915 (2005).
27. L. Helfen, F. Xu, H. Suhonen, P. Cloetens, T. Baumbach, Laminographic imaging using synchrotron radiation–challenges and opportunities. *J. Phys. Conf. Ser.* **425**, 192025 (2013).
28. Y. Yang et al., Quantification of heterogeneous degradation in Li-ion batteries. *Adv. Energy Mater.* **9**, 1900674 (2019).
29. B. D. Lucas, T. Kanade, "An iterative image registration technique with an application to stereo vision" in *IJCAI'81: Proceedings of the 7th International Joint Conference on Artificial Intelligence - Volume 2* (Morgan Kaufmann Publishers Inc., 1981), pp. 674–679.
30. J. Li et al., Multiphase, multiscale chemomechanics at extreme low temperatures: Battery electrodes for operation in a wide temperature range. *Adv. Energy Mater.* **11**, 2102122 (2021).
31. Y. Qi, S. J. Harris, In situ observation of strains during lithiation of a graphite electrode. *J. Electrochem. Soc.* **157**, A741 (2010).
32. S. Schweidler et al., Volume changes of graphite anodes revisited: A combined operando X-ray diffraction and in situ pressure analysis study. *J. Phys. Chem. C* **122**, 8829–8835 (2018).
33. P. Pietsch et al., Quantifying microstructural dynamics and electrochemical activity of graphite and silicon-graphite lithium ion battery anodes. *Nat. Commun.* **7**, 12909 (2016).
34. R. Xu et al., A morphologically stable Li/electrolyte interface for all-solid-state batteries enabled by 3D-micropatterned garnet. *Adv. Mater.* **33**, e2104009 (2021).
35. C. R. Birkl, M. R. Roberts, E. McTurk, P. G. Bruce, D. A. Howey, Degradation diagnostics for lithium ion cells. *J. Power Sources* **341**, 373–386 (2017).
36. R. Jung et al., Nickel, manganese, and cobalt dissolution from Ni-rich NMC and their effects on NMC622-graphite cells. *J. Electrochem. Soc.* **166**, A378 (2019).
37. H. Charalambous et al., Comprehensive insights into nucleation, autocatalytic growth, and stripping efficiency for lithium plating in full cells. *ACS Energy Lett.* **6**, 3725–3733 (2021).
38. T. Buzug, *Computed Tomography: From Photon Statistics to Modern Cone-Beam CT* (Springer Belin, Heidelberg, ed. 1, 2008), p. 522.
39. G. Zan et al., In situ visualization of Li-whisker with grating-interferometry-based tricontrast x-ray microtomography. *ACS Mater. Lett.* **3**, 1786–1792 (2021).
40. M. Holler et al., Three-dimensional imaging of integrated circuits with macro-to nanoscale zoom. *Nat. Electron.* **2**, 464–470 (2019).
41. N. S. O'Brien, R. P. Boardman, I. Sinclair, T. Blumensath, Recent advances in X-ray cone-beam computed laminography. *J. XRay Sci. Technol.* **24**, 691–707 (2016).
42. G. Zan et al., High-resolution multicontrast tomography with an X-ray microarray anode-structured target source. *Proc. Natl. Acad. Sci. U.S.A.* **118**, e2103126118 (2021).
43. Z. Wei et al., A micro-CL system and its applications. *Rev. Sci. Instrum.* **88**, 115107 (2017).
44. H. Deyhle et al., Spatial resolution of a laboratory based X-ray cone-beam laminography scanning system for various trajectories. *NDT Int.* **111**, 102222 (2020).
45. T. M. M. Heenan et al., Theoretical transmissions for X-ray computed tomography studies of lithium-ion battery cathodes. *Mater. Des.* **191**, 108585 (2020).
46. M. Feser et al., Sub-micron resolution CT for failure analysis and process development. *Meas. Sci. Technol.* **19**, 094001 (2008).
47. A. P. Merkle, J. Gelb, The ascent of 3D X-ray microscopy in the laboratory. *Micros. Today* **21**, 10–15 (2013).